Design of a cone-cylinder-flare configuration for hypersonic boundary-layer stability analyses and measurements with attached and separated flows

Sebastien Esquieu, Steven P Schneider, Elizabeth K Benitez, Jean-Philippe Brazier

Association Aéronautique et Astronautique de France

57th 3AF International Conference on Applied Aerodynamics
29 — 31 March 2023, Bordeaux – France

AERO2023-51-ESQUIEU

DESIGN OF A CONE-CYLINDER-FLARE CONFIGURATION FOR HYPERSONIC BOUNDARY-LAYER STABILITY ANALYSES AND MEASUREMENTS WITH ATTACHED AND SEPARATED FLOWS

Sebastien Esquieu[1], Steven P. Schneider[2], Elizabeth K. Benitez[3], Jean-Philippe Brazier[4]

[1]*CEA, The French Alternative Energies and Atomic Energy Commission, Le Barp, France, sebastien.esquieu@cea.fr*

[2]*School of Aeronautics and Astronautics, Purdue University, West Lafayette, Indiana, USA*

[3]*US Air Force Research Laboratory, Wright-Patterson Air Force Base, OH, 45433*

[4]*ONERA / DMPE, Université de Toulouse, F-31055 Toulouse - France*

ABSTRACT

The stability of hypersonic boundary-layer over axisymmetric cone-cylinder-flare configurations at Mach 6 and zero degree angle of attack is investigated for different Reynolds numbers. The shapes have been specifically designed for wind tunnel test experiments to create well suited geometries for hypersonic laminar-turbulent transition analyses with attached and separated flows taking into account the effects of pressure gradients, flow expansion and recompression, on the hypersonic boundary-layer stability.

After a thorough study of the aerodynamic flows obtained in fully laminar conditions on each configuration, linear stability theory (LST) and linear parabolized stability equations (PSE) are used to predict the amplification rates of the boundary-layer disturbances for the case without flow separation. The numerical stability results are compared to wind tunnel measurements obtained in the BAM6QT (Boeing AFOSR Mach-6 Quiet Tunnel) wind tunnel. The semi-empirical e^N method allows to correlate transition with the integrated growth of the linear instability waves.

Nomenclature

$Mach$	Mach number
pi	stagnation pressure (bar)
Ti	stagnation temperature (K)
Hi	total enthalpy (J/kg)
p	static pressure (Pa)
T	static temperature (K)
ρ	density (kg/m^3)
u,v,w	velocity in x,y,z directions (m/s)
V	velocity magnitude
$Re_{/m}$	freestream unit Reynolds number (1/m)
x	geometric coordinate in streamwise direction (m)
y	geometric coordinate in radial direction (m)
Rn	nose radius (m)
δ	boundary-layer thickness (m)
α_i	amplification rate (1/m)
ψ	wave propagation angle (^{o})

Subscript

∞	value in freestream
e	value at the boundary-layer edge

1. INTRODUCTION

The laminar-to-turbulent transition is a primordial input for trajectory and conceptional design of hypersonic objects. Indeed, transition at hypersonic speeds causes large changes in heat transfer, skin friction and boundary-layer separation. Turbulent boundary-layers increase the heating rate and the viscous drag, and offer a greater resistance to the formation of separation bubbles. As a consequence, the aerodynamic lift and drag, the stability and control of the object as well as the thermal protection system are directly affected by the state of the boundary-layer. So the knowledge of stability and transition of high-speed boundary-layers is an important issue for hypersonic flights. But understanding how and where transition occurs on a given configuration during

re-entry or high speed flight is one of the long-standing problems in aerodynamics (Leyva [11]).

In flight or in a wind tunnel, disturbances are present in the flow and interact with the boundary-layer that develops along the object. The boundary-layer acts as a selective filter where only certain frequencies and wavelengths of those disturbances can be amplified and eventually induce a laminar-to-turbulent transition. For a small disturbance environment, as explained by Stetson [22], four fundamentally different instability mechanisms can produce disturbance growth in a hypersonic boundary-layer: first-mode, second mode, crossflow instabilities and Görtler vortices. Several paths to transition exist (Morkovin [17]) but, here, only the low disturbance level is considered where eigenmode growth is dominant.

As detailed by Schneider [20], the first-mode instability is similar to low-speed Tollmien-Schlichting waves and occurs for subsonic and moderate supersonic flows. It is most amplified when the wavefronts are oblique to the stream direction. The second mode instability concerns hypersonic flows. It is similar to a trapped acoustic wave and is most amplified when the wavefronts are normal to the stream direction. The cross-flow instability occurs in three-dimensional boundary-layers, and has both traveling and stationary forms. The Görtler instability is important for boundary-layers on concave walls, and perhaps in some regions of concave streamline curvature.

Very instructive and thorough studies of the transition development are available for attached boundary-layer mainly on conical shapes. Here the cone-cylinder-flare configurations add the influence of pressure gradients, flow expansion and compression, on the boundary-layer stability. Different flare angles are used in order to generate different levels of compression: a limited pressure gradient to keep an attached boundary-layer (Esquieu [7]) and a higher adverse pressure gradient to generate a flow separation (Benitez [3]).

The hypersonic flows addressed here are considered in wind tunnel conditions at Mach 6. In these high speed conditions and with the quasi-sharp cone-cylinder shape, the edge Mach number will be greater than Mach 5 all along the configuration. Following Mack's theory [15], for the attached boundary-layer case the dominant instabilities will be the second mode waves. Other instabilities such as Görtler instabilities could also be present in the concave part of the geometry. For small flare angle, these instabilities should not be predominant. But for larger flare angles with a separation bubble, Görtler instabilities, streaks or even other instability mechanisms should be considered for the study of the transition process. Such studies have been conducted on a hollow cylinder flare configuration first by Benay [1] and Bur [5], and more recently by Lugrin [13] [14].

The detailed stability analysis of the cone-cylinder-flare shape with a larger flare angle with flow separation is out of the scope of this paper. Nevertheless this case is the object of recent studies and is still under investigation (Paredes [18], Li [12], Benitez [2], Caillaud [6]).

2. CONE-CYLINDER-FLARE GEOMETRIES

Axisymmetric cone-cylinder-flare configurations (see figure 1) were designed in order to promote transition development for attached and detached boundary-layers with expansion and recompression in high speed flow [7].

The main characteristics of the designed shape are the following:

- small nose radius Rn = 0.1 mm ;
- half-cone angle equal to 5 degrees ;
- cylinder at 0 degree on the central part ;
- flare angles:
  - $\Rightarrow$ 3.5 degrees (CCF3-5 configuration) ;
  - $\Rightarrow$ 10 degrees (CCF10 configuration).

CCF3-5 has been designed to keep an attached boundary-layer whereas CCF10 allows to generate a significant flow separation at the cone-flare junction.

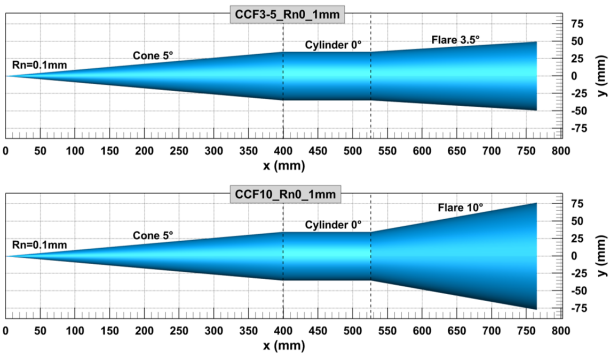

Figure 1: The CCF3-5 and CCF10 cone-cylinder-flare geometries

The main dimensions of the cone-cylinder-flare configurations, CCF3-5 and CCF10, are given in table 1.

Table 1: CCF3-5 and CCF10 model coordinates

	Nose-Cone junction	Cone-Cylinder junction	Cylinder-Flare junction
x (mm)	92.0×10^{-3}	398.15	525.67
y (mm)	99.7×10^{-3}	34.93	34.93

In order to promote the flow separation development

and the amplification of laminar-turbulent transition instabilities, a third geometry called CCF12 has been defined based on the results obtained in [7], [3] and [18]. This CCF12 shape has a longer cylinder (extended to x=546.61m) and a larger flare angle equal to 12° (see figure 2). This geometry is currently under study by partners, this configuration is not analyzed in this paper.

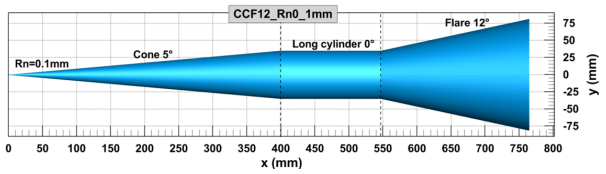

Figure 2: The CCF12 cone-cylinder-flare geometry

3. STRUCTURED GRIDS

For the CCF3-5 configuration, the initial grid is a single-block structured grid composed of 1009 points in the longitudinal direction and 301 points in the wall normal direction. The initial grid can be qualified as very good quality (see top figure 3) but in order to ensure higher accuracy of the mean flow solution for the stability analysis, the shock tailoring procedure is used. This grid adaptation procedure allows to capture all the gradients precisely by redistributing the grid points based on the initial converged solution (see bottom figure 3).

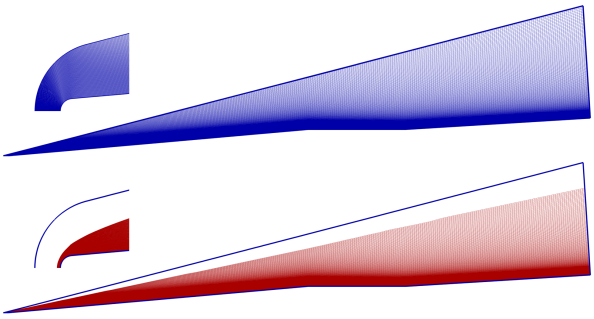

Figure 3: CCF3-5 configuration - Initial and tailored grids (Mach=6 - $Re_{/m}$ = 5.6x10^6) (1009 x 301)

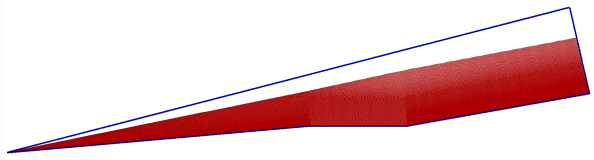

Figure 4: CCF10 configuration - Initial (edge only) and tailored grid (Mach=6 - $Re_{/m}$ = 11.2x10^6) (2311 x 401)

The CCF10 grids (initial and tailored) presented in figure 4 are made of 2311 x 401 grid points. Following a grid convergence process, the required number of points is important. Indeed the flow separation region is a complex zone that needs a very high refinement level to capture efficiently the complex physics: separation bubble, induced shock as well as reattachment shock among others (see figure 7 for physical details).

4. CFD COMPUTATIONS

4.1 Laminar mean flow computations

The laminar mean flow solutions are performed with the axisymmetric CFD code provided with the STABL software suite written by Dr. Johnson [9]. This axisymmetric flow solver DPLR2D uses a finite volume formulation and solves the reacting Navier-Stokes equations. The second-order inviscid fluxes are based on the modified Steger-Warming flux vector splitting method. The viscous fluxes are also second-order accurate. The time integration method is the implicit first-order data parallel line relaxation (DPLR) method.

Since the aerodynamic flows considered here correspond to cold wind tunnel conditions in air, the gas mixture considered for the computation is non-reacting gas "Air" (perfect gas) and the effects of chemistry and molecular vibration are omitted for the calculations. The main freestream aerodynamic conditions used for the computations presented here are given in table 2. The viscosity law used is Sutherland's law and the heat conductivity is calculated using Eucken's relation.

Table 2: Aerodynamic conditions (1/2)

Case	Mach	pi (bar/psia)	Ti (K)	$Re_{/m}$	p_∞ (Pa)
1	6.0	2.59 / 37.5	430.	2.8x10^6	164.0
2	6.0	5.17 / 75.0	430.	5.6x10^6	327.5
3	6.0	10.34 / 150.0	430.	11.2x10^6	654.9

The laminar mean flow solutions obtained on the CCF3-5 and CCF10 geometries at $Re_{/m}$ = 11.2x10^6 are presented in figure 5 as pseudo-schlieren visualizations. The density gradient magnitude shows the bow shock generated from the small nose radius of 0.1 mm, the boundary-layer with a sensitive increase on the cylinder part due to the flow expansion and finally the effect of the adverse pressure gradient on the flare.

There is a dramatic effect of the flare angle on the boundary-layer:

- CCF3-5: the limited recompression generated by the flare can be handled by the incoming boundary-layer on the cylinder. The flow stays attached to the wall on the cylinder and on the flare ;

- CCF10: the boundary-layer is still attached just after the cone-cylinder junction but can not handle the adverse pressure gradient generated by the 10 degrees flare. The boundary-layer separates from the wall - a large separation bubble is generated.

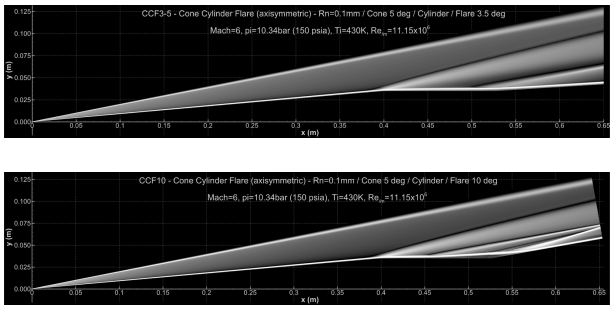

Figure 5: CCF3-5 and CCF10 configurations - Density gradient magnitude at $\mathrm{Re}_{/m}$ = 11.2x10^6

4.2 Flow analysis

4.2.1 Flow around the nose

From a stability analysis point of view, it is known that the increase of the bluntness of the nose (untill a given limit to avoid the blunt-body paradox) has a stabilizing effect on the boundary-layer [21]. Indeed, in hypersonic flow, increasing nose bluntness pushes back the point where second mode disturbances become active. Here, the cone has a quasi-sharp nose ($R_n = 0.1mm$) so it is very favorable to develop second mode instabilities along the cone.

For the accuracy of the stability analysis study, it was decided to give special attention to the nose region in the computations. For this perfect-gas flow, the Mach number distribution around the stagnation point is presented in figure 6 for two Reynolds numbers.

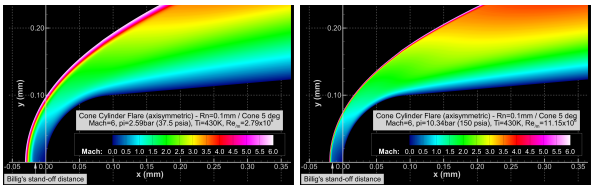

Figure 6: Mach number distribution around the nose at $\mathrm{Re}_{/m}$ = 2.8x10^6 and $\mathrm{Re}_{/m}$ = 11.2x10^6

The high gradients around the nose are very accurately captured by the computations thanks to the fine initial grids used and to the grid tailoring procedure. So the influence of this very small bluntness is thoroughly defined for stability analysis purposes.

4.2.2 Flow separation

As indicated previously, the 10 degrees flare angle generates an important flow separation at the junction of the cylinder and the flare as illustrated in figure 7.

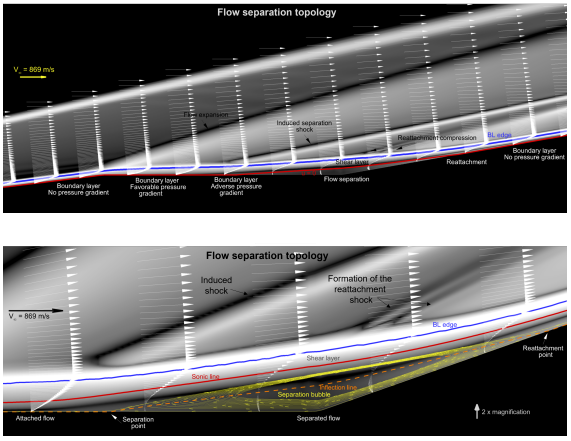

Figure 7: Physics of the flow separation region

Listed below is a short description of the flow separation zone:

- Because of the presence of the separation bubble, an induced shock is generated near the separation point leading to a local pressure increase ;
- Inside the bubble, the velocity profiles are strongly modified and negative values appear in the lower part of the bubble below the inflection line ;
- Upstream of the reattachment point, a recompression shock is gradually forming leading to local high pressure gradient on the flare ;
- The rapid change of the boundary-layer properties in this reattachment region leads to high heat flux values at the reattachment point where the boundary-layer thickness reaches a minimum ;
- Above the bubble, the mixing layer is known to be a region of important instability amplifications leading to abrupt laminar-turbulent transition breakdown under some conditions.

The complexity of the separation region gives an idea why laminar-turbulent transition prediction in the presence of hypersonic flow separation is one of the long-standing problem for high speed flows.

4.2.3 Pressure and skin friction

The case with attached boundary-layer (CCF3-5)

On cone-cylinder-flare geometry, the flow encounters not only the classical quasi-constant pressure level on the cone but also experiences pressure gradients further downstream: firstly a favorable pressure gradient on the cylinder and secondly an adverse pressure gradient on the flare as shown in figure 8.

The skin friction constantly diminishes on the cone and, after a narrow peak at cone-cylinder junction, experiences a new significant decrease on the cylinder (see figure 8). The minimum skin friction value at the cone-flare junction is followed by a slight and progressive increase on the flare.

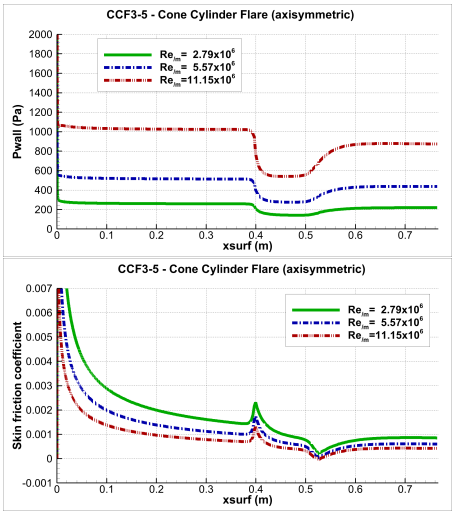

Figure 8: CCF3-5 - Pressure and skin friction distribution

As stated previously, near the cylinder-flare junction the flow faces an adverse pressure gradient due to the presence of the flare. This generates a dynamic situation where the flux of the incoming fluid momentum will eventually be balanced by the force and the flow will be brought to rest [23]. In this situation, a sufficient pressure gradient will lead to a flow separation.

Here the CCF3-5 shape has been designed with a small flare angle in order to generate a limited adverse pressure gradient so that no separation bubble appears. It is confirmed that the boundary-layer is still attached. It can be noticed nevertheless that the skin friction coefficient is close to zero at the cylinder-flare junction. The addition of the wall shear stress and the positive pressure increase is not sufficient to generate a back-flow region but it can be stated that any increase of the flare angle will lead to the formation of a separation bubble. This is exactly the case when increasing the flare angle to 10 degrees on the CCF10 configuration.

The case with flow separation (CCF10)

The effect of flow separation on the pressure and skin friction is illustrated on figure 9. The shock induced by the separation leads to a pressure increase followed by a pressure plateau. The recompression moves downstream near the reattachment point and is visible as a strong pressure gradient on the flare. The skin friction is now negative over the extent of the separation bubble.

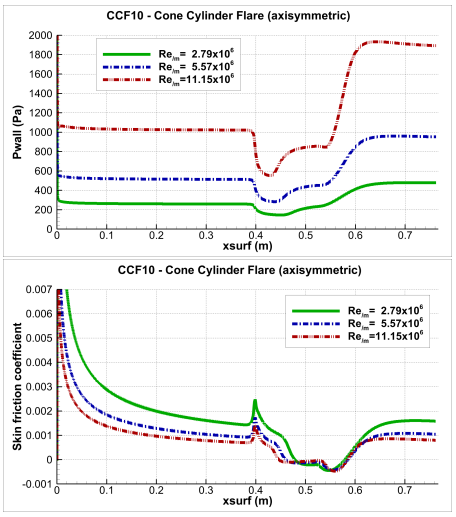

Figure 9: CCF10 - Pressureand skin friction distribution

It is known that separated flows lead to brutal laminar-turbulent transition breakdown and that instability mechanisms are amplified in the mixing layer above the bubble. There is still some unknowns about the physical processes leading to the transition and the type of mechanisms that develop on hypersonic separated flows.

4.2.4 Boundary-layer properties

The boundary-layer detection is never a trivial calculation for hypersonic flows. Here the detection is based on the “Return from enthalpy overshoot“ criterion. For this criterion, the total enthalpy at the boundary-layer edge satisfies:

$$Hi_e < \frac{Hi_\infty - Hi_{wall}}{0.995} + Hi_{wall}$$

The resulting boundary-layer thicknesses are presented in figure 10. Whatever the Reynolds number considered, the general trend of the boundary-layer thickness evolution is the same. After the classical increase of the boundary-layer thickness along the cone, a new abrupt and large thickness increase appears on the cylinder because of the influence of the flow expansion generated at cone-cylinder junction. Downstream of this point, two different cases appears depending on the configuration:

- CCF3-5: the adverse pressure gradient leads to an important decrease of the boundary-layer thickness on the first half of the flare before a slight increase of the boundary-layer thickness further downstream ;

- CCF10: the separation bubble is a large zone which leads to a high increase of the boundary-layer thickness knowing that a mixing layer develops above the recirculation region. The physics is dramatically different between the attached case and the separated one - a larger distance above the wall is concerned by viscous effects. The increase of Reynolds number thickens the boundary-layer

and changes the length of the separation bubble (longer for high Reynolds number for these laminar solutions).

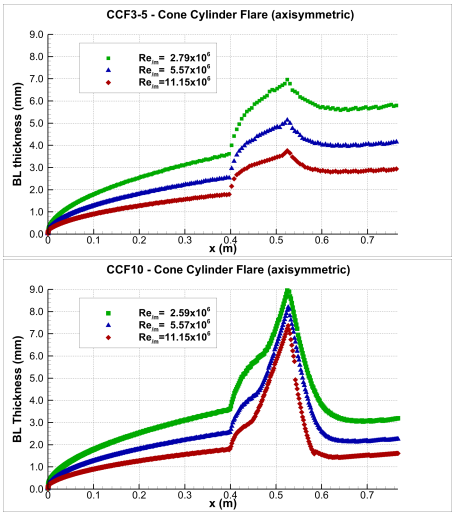

Figure 10: CCF3-5 / CCF10 - Boundary-layer thickness

The parallel flow assumption necessary to apply LST and PSE analysis is no longer valid for separated flows. The analysis of such flows requires more advanced tools (global stability, HLNSE, DNS [12] [13] [6]) which are not in the scope of the present study based on local stability theory **so the stability of the case with flow separation is not analysed in this paper**.

5. STABILITY ANALYSES ON THE ATTACHED BOUNDARY-LAYER CASE

The edge Mach number values detected with the total enthalpy criterion in the computations are shown in figure 11. The value of $M_e \sim 5.5$ on the cone is in good agreement with the Taylor-Maccoll estimation of $M_e \sim 5.6$ for a 5-degrees half-angle nearly-sharp cone at a freestream Mach number of 6.0 at moderate Reynolds numbers. Downstream, the edge Mach number increases to around $M_e \sim 6.1$ on the cylinder due to the flow expansion and finally decreases to around $M_e \sim 5.65$ on the flare after the recompression at the cylinder flare junction.

It is known that the second mode instabilities grow more rapidly at high Mach number values and on cold walls. Here, the high edge Mach number and the limited wall temperature ($T_{wall} \sim 300K$) suggest that the second mode waves will be the dominant instability as stated by Mack's theory [15]. Furthermore, knowing that second mode instability frequencies are directly linked to the boundary-layer thickness, it can be guessed that very different frequencies will be amplified on the different parts of the object.

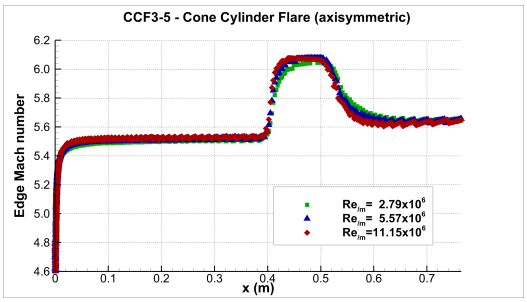

Figure 11: CCF3-5 - Edge Mach number

5.1 First and Second mode instabilities

Mack [15] found that the major instability waves leading to transition to turbulence on a smooth flat plate in a perfect gas flow are the first and second modes.

First-mode instabilities
In a supersonic flow, the most unstable first-mode disturbance is always oblique (ψ=45-60°). The wave angle ψ of the most unstable disturbance increases rapidly with Mach number and is in the range from 55°-60° above a Mach number of 1.5.

Second-mode instabilities
In hypersonic flows above an edge Mach number of 4.5, the second mode is the most unstable - these waves are most unstable as two-dimensional disturbances (ψ=0 °). The second mode waves are acoustic instabilities propagating and growing inside the laminar boundary-layer and their final breakdown leads to turbulent flow. The boundary-layer behaves as an acoustic waveguide as indicated by Fedorov [8]. Knowing that the wavelength of the second mode instability is about twice the boundary-layer thickness [10], the estimated second mode instability frequency is calculated as:

$$f_{second\,mode} = \frac{V_e}{2\delta}$$

So for waves moving with the edge velocity ($V_e \sim 860m/s$), the estimated frequency of the second mode wave disturbance will be respectively of the order of 240 kHz at the end of the cone for the thin boundary-layer ($\delta \sim 1.8mm$) at $\mathrm{Re}_{/m}$ =11.2x10^6 and 120 kHz for the thicker one ($\delta \sim 3.6mm$) at $\mathrm{Re}_{/m}$ = 2.8x10^6.

On the cone-cylinder-flare configurations, complementary analyses (not presented here) have confirmed that the first and second-mode waves have both similar energy levels on the first two thirds of the conical part. Downstream of this zone, the second-mode, better tuned to the boundary-layer thickness, shows an increased growth that leads to its dominance at the end of the cone. **So here for this attached boundary-layer case (CCF3-5), the focus**

is only on the second mode waves with particular attention to the influence of pressure gradients on the development of these instabilities. For flow separated cases (CCF10 / CCF12), the first-mode should also be looked at carefully because of possible interactions with the bubble region.

5.2 Stability analysis solvers

5.2.1 STABL

The main part of the stability analyses are performed using the PSE-Chem solver, which is a part of the STABL software suite [9]. PSE-Chem solves the reacting, two-dimensional, axisymmetric, linear parabolized stability equations (PSE) to predict the amplification of disturbances as they interact with the boundary-layer. The PSE-Chem solver includes finite-rate chemistry and translational-vibrational energy exchange. Both linear stability theory LST and PSE analyses were performed using the PSE-Chem code.

5.2.2 Mamout

Stability analyses have also been carried out on the same configuration with the ONERA in-house code Mamout. This code solves the local linear stability equations for an incompressible fluid, an ideal gas or a chemical equilibrium mixture, with the parallel flow assumption. The present computations use the perfect gas model. The resulting one-dimensional differential eigenvalue problem can be solved thanks to several numerical schemes, among which are the Chebyshev polynomial collocation method and high-order compact schemes. The computational grid can be split in multiple sub-domains. Outside of the boundary-layer, the fluctuation is matched to the analytical solution obtained for a uniform base flow.

The same DPLR2D laminar flow solutions are used as input for STABL and Mamout stability analyses.

5.3 Stability analysis results

The second mode disturbances are highly ”tuned” to the boundary-layer thickness resulting in considerable selectivity in the disturbance frequencies which are most amplified [22]. Seeing the boundary-layer thickness evolution shown in figure 10, it has been stated that the thin boundary-layer on the cone will generate higher frequency disturbances than the thicker boundary-layer on the cylinder and on the flare. Here, another aerodynamic effect will impact the boundary-layer stability: the pressure gradients generated respectively on the cylinder and on the flare.

5.3.1 Amplification rates

The stability diagrams presented in figure 12 show the standard ”thumb” curve on the cone. The higher frequencies at the beginning of the cone detune rapidly in the narrow amplified band but, as the disturbance waves proceed more downstream, they become better tuned to the boundary-layer thickness and amplify at important rates on longer periods of growth. As a consequence, the resulting amplified boundary-layer instabilities can reach high amplitude on the cone potentially leading to the critical breakdown amplitude for moderate to high Reynolds numbers.

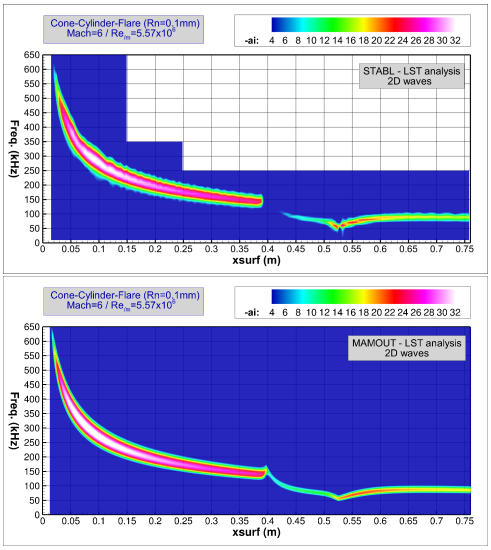

Figure 12: Amplification rates from STABL and Mamout LST analyses at $\mathrm{Re}_{/m} = 5.57\mathrm{x}10^6$

Concerning the cylinder part, it is known that a favorable pressure gradient has a stabilizing effect on the boundary-layer. This is definitively confirmed by the stability diagrams where no substantial amplification rates are visible on the main part of the cylinder. As shown in figures 10, the boundary-layer thickens very rapidly under the influence of the flow expansion and experiences a very rapid change all along the cylinder. The “accelerated“ boundary-layer is very stable as confirmed by the amplification rate diagrams.

The phenomenon is totally different on the flare and it is interesting to restate here that adverse pressure gradients are commonly known as destabilizing for the boundary-layer. The boundary-layer thins rapidly just after the cylinder-flare junction but, once past the pressure gradient, the boundary-layer keeps a quite constant thickness and a quite identical profile all along the flare. As a consequence, it can be guessed that, after an important destabilization at the cylinder-flare junction, a quite amplified frequency “plateau“ could be

observed on the flare. This is confirmed by figure 12. The amplified waves stay in a narrow frequency range on the flare which can potentially generate high amplitude disturbances at the end of the flare. These general trends are confirmed with the code-to-code comparison, STABL / Mamout, which points out a good agreement between these two numerical approaches. This verification gives an even larger confidence in the numerical predictions.

The Reynolds effect on the amplification of the second mode frequency waves is clearly highlighted by figure 13. This higher Reynolds number leads logically to high frequency content: 200 to 1000 kHz on the cone and a long flat frequency range on the flare around 120-130 kHz with high amplification rate levels.

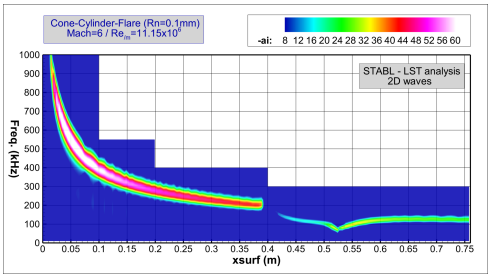

Figure 13: Amplification rates from STABL-LST analyses at $Re_{/m}$ = 11.2x10^6

5.3.2 N-factors

Knowing the evolution of an initial disturbance as it moves downstream from its starting point through the mean flowfield, the onset of transition can be estimated with the semi-empirical e^N correlation method. In PSE-Chem, the N factor is defined as:

$$N = \int_{s_0}^{s} [-\alpha_i + \frac{1}{2E}\frac{dE}{ds}]ds$$

where not only the imaginary component of the streamwise wavenumber is taken into account (as in LST) but also the change in the kinetic energy of the shape function.

With this integrated growth of the linear instability waves, it is possible to correlate the onset of transition using N-factor values of about 8-11 for quiet tunnel and flight environments and levels around 4 to 5 for conventional tunnels with larger freestream noise environment.

N factor distribution at $Re_{/m}$ =5.6x10^6 obtained in PSE mode for the two-dimensional disturbances only (ψ= 0°) are shown in figure 14. For this intermediate Reynolds number, N factors slightly lower than 5 are reached at the end of the cone and slightly greater than 5 at the end of the model. Such N factors values can conduct to turbulent breakdown in a noisy environment while quiet experiments should detect important waves amplitudes before critical laminar-to-turbulent breakdown.

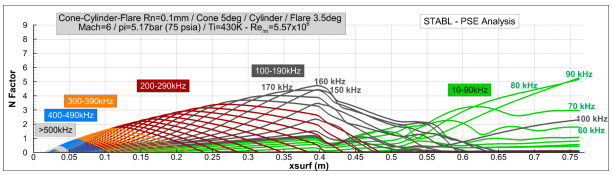

Figure 14: N factors by frequency from STABL-PSE analysis at $Re_{/m}$ = 5.6x10^6

At $Re_{/m}$ = 11.2x10^6, high N factor values are reached: around 8 at the end of the cone and almost 9 at the end of the flare. **This case would be turbulent in noisy conditions but represents an ideal candidate for quiet experiments**. Indeed, in quiet tunnel conditions, without noise radiated from the boundary-layers on the nozzle walls, this case will generate critical wave amplitudes, very near to transition breakdown or possibly turbulent at the end of the configuration.

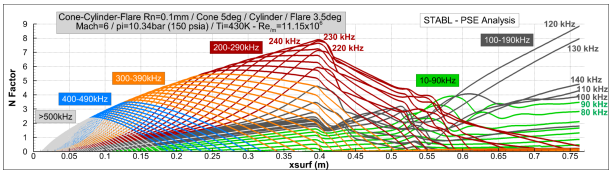

Figure 15: N factors by frequency from STABL-PSE analysis at $Re_{/m}$ = 11.2x10^6

In parallel of these numerical studies, experiments have been realized in the BAM6QT wind tunnel on this shape. Several runs have been obtained respectively in noisy and in quiet conditions. In order to compare the previous numerical analysis to experimental results, comparisons on two noisy runs are presented in the next chapter.

6. MODEL AND EXPERIMENTS

6.1 The CCF3-5 cone-cylinder-flare model

The cone-cylinder-flare model CCF3-5 has been produced in the Aerospace Sciences Laboratory of Purdue University. The model is divided into three sections: a stainless steel nose tip, an aluminum mid-body containing the initial 5 degrees cone and the first half of the cylinder, and an aluminum base including the latter half of the cylinder and the 3.5 degrees conical flare (see figure 16). The nose tip was made to be as sharp as could be produced with a nose radius equal to 0.1mm based on microscope visual inspection.

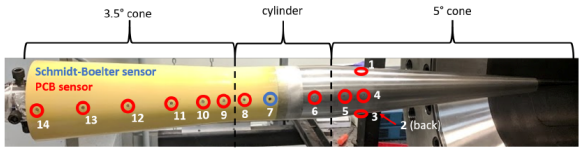

Figure 16: Purdue model with PCB sensors for BAM6QT experiments

PCB132B38 sensors are used for the measurement of the pressure fluctuations relative to the development of boundary-layer instabilities.

6.2 Boeing / AFOSR Mach-6 Quiet Tunnel

Experimental tests were conducted in Purdue University's Boeing/Air Force Mach 6 Quiet Tunnel. The BAM6QT is a Ludwieg tube, a long tube with a converging-diverging nozzle on the end (see figure 17). The flow passes from the driver tube, through the test section, diffuser, a second throat, and finally to the vacuum tank. More details about the BAM6QT wind tunnel can be found in [19].

BAM6QT can be operated as a conventional noisy tunnel or as a quiet tunnel. Flow is initiated by bursting a double diaphragm that is located downstream of the diffuser. Run times of 3-5 s are typical. The tunnel uses air as the test gas and operates with an initial stagnation pressure of 34-2070 kPa (0.34-20.7 bar) and an initial stagnation temperature of 430 K, giving a $Re_{/m}$ range of 0.36-22.3 x 10^6.

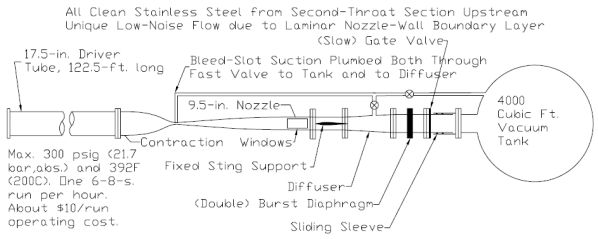

Figure 17: Schematic of BAM6QT

Quiet and noisy runs have been realized, here the focus is on two noisy runs for boundary-layer stability analysis and numerical / experimental cross-comparisons.

6.3 Comparison of STABL analyses and BAM6QT measurements

6.3.1 Noisy runs

Two noisy runs are considered for the numerical / experimental comparison respectively at $Re_{/m}$ = 3.3x10^6 and $Re_{/m}$ = 6.0x10^6. In noisy environment, the experimental Mach number is equal to 5.8 because of the larger turbulent boundary-layer thickness which develops on the nozzle walls in these conditions (reduction of the apparent nozzle exit diameter). The corresponding aerodynamic conditions are given in Table 3:

Table 3: Aerodynamic conditions

Run	Mach	pi (bar/psia)	Ti (K)	$Re_{/m}$
Run25	5.8	2.85 / 41.3	430.	3.31x10^6
Run18	5.8	5.17 / 75.0	430.	6.00x10^6

These aerodynamic conditions are not exactly the ones corresponding to the numerical cases presented previously in the paper at Mach 6, so new STABL computations have been performed at Mach 5.8.

Figure 18 shows comparisons of measured power spectra with computed N factors at 5 x-locations. Indeed, the N factor corresponds roughly with wave amplitude since it is a representation of how much a wave has grown along the body (Berridge et al. [4]). The initial amplitude of the wave is not known so this N factor can not give an absolute wave amplitude. Nevertheless figure 18 displays such N factor / power spectra comparison for the two noisy runs considered here. The overall agreement is correct.

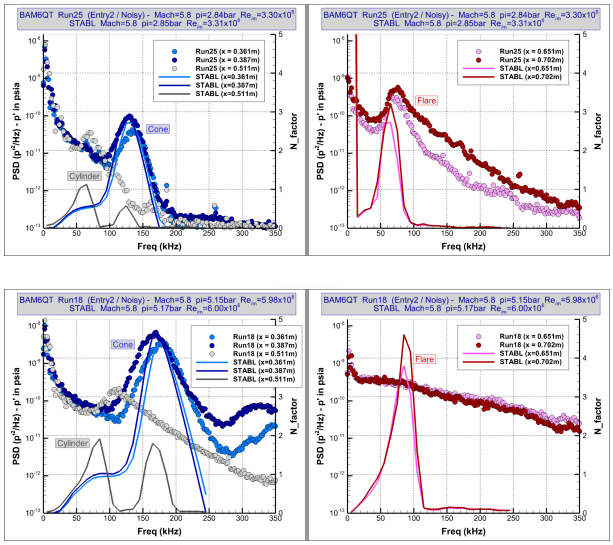

Figure 18: BAM6QT PSD data for noisy runs and STABL N-factors at $Re_{/m}$ = 3.3x10^6 and $Re_{/m}$ = 6.0x10^6

On the cone, second mode waves can be seen on each PCB sensor location (x=0.361m and x =0.387m). Excellent agreement is obtained with the STABL N factors adjusted manually to fit with the experimental power spectra amplitudes. For these noisy runs, the power spectra indicate that the boundary-layer remains laminar

on the cone. A new increase of the Reynolds number (above 6 million) should lead to a turbulent spectrum knowing that the onset of transition can be estimated using N factor values around 4 to 5 for conventional noisy runs.

On the cylinder part, the computed / experimental comparison is not as evident as on the cone. At the considered PCB location (x=0.511m) just before the end of the cylinder, two peaks can be observed on the N factor prediction but only one on the experimental power spectra. As visible in figure 19, the two peaks computed with STABL at $Re_{/m}$ = 6.0x10^6 come respectively from the second mode waves highly amplified on the cone at 170 kHz progressively damped on the cylinder part and to lower frequencies at around 70-90 kHz amplified along this second section of the object. The peak detected in the experiment is at 110 kHz, so at a higher frequency than the numerical prediction. The measured / computed comparison is inconclusive on this cylinder part.

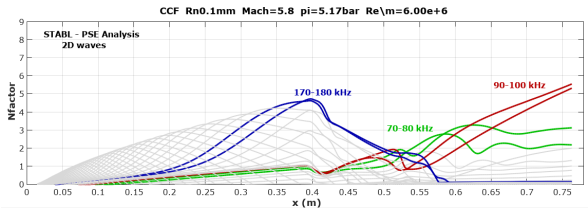

Figure 19: STABL N factors at $Re_{/m}$ = 6.0x10^6

On the flare, the boundary-layer is laminar at $Re_{/m}$ = 3.3x10^6 with experimental second mode peaks observed at around 70 and 75 kHz. The computed frequencies are at a slightly lower frequency. For the second run at $Re_{/m}$ = 6.0x10^6, the PCB measurements indicate a turbulent spectrum on the flare while the stability analysis indicates N factors at around 4.5 for wave frequencies around 90 kHz. In noisy conditions, such N factor values are indeed near to transition. Here the flow has become turbulent on the flare even if the predicted N factor is slightly lower on the flare than on the cone - this fact is questionable. One possible explanation could be that in experiments an increased tunnel noise exists at lower frequencies while a decreased tunnel noise is observed at high frequency (see Marineau et al. [16]). So the transition could appear earlier on the lower frequency band on the flare than on the higher frequency band on the cone.

6.3.2 Quiet runs

Quiet runs have also been realized as presented in [7] and [3]. Comparisons with STABL instability computations can not be added to this short paper, this will be done in an extended version to be published soon.

7. PERSPECTIVES ON THE SEPARATED BOUNDARY-LAYER CASES (CCF10 AND CCF12)

The two configurations CCF10 and CCF12, not analyzed in this paper from a stability point of view, are the object of several recent and upcoming studies [18] [12] [2] [6]. Wind tunnel tests at ONERA-R2Ch (see figure 20) and numerical studies are currently conducted on the CCF12 model in a CEA-ONERA collaboration. This configuration is also studied in the framework of a NATO group (NATO-AVT-346).

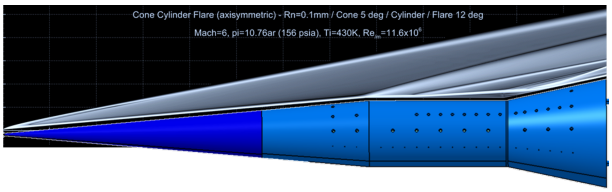

Figure 20: CCF12 model for R2Ch wind tunnel tests

8. CONCLUSION

The cone-cylinder-flare configurations, CCF3-5, CCF10 and CCF12, generate very interesting aerodynamic flows for the study of hypersonic boundary-layer stability in presence of pressure gradients.

The increase of the flare angle to 10 degrees, or even better to 12 degrees, provide an excellent candidate for the study of the long-standing problem of the understanding of laminar-turbulent transition breakdown in the presence of a hypersonic flow separation. In that sense, these configurations, well suited to wind tunnel tests, are a real asset for the study of hypersonic transition in the presence of a flow separation.

Aerodynamic breakthrough on these cone-cylinder-flare configurations could be very useful in the global effort to evaluate more accurately how the state of the boundary-layer affects the aerodynamic lift and drag, the stability and control as well as the thermal protection system for even more complex hypersonic 3D shapes.

9. ACKNOWLEDGMENTS

Sebastien Esquieu thanks Professor Steven P. Schneider, Elizabeth Benitez and Jean-Philippe Brazier for this very rich collaborative work. Many thanks also to Heath Johnson from University of Minnesota for the access to the STABL suite.

REFERENCES

[1] R. Benay, B. Chanetz, B. Mangin, Vandomme L., and J. Perraud. Shock wave/transitional boundary layer interactions in hypersonic flow. *AIAA Journal, Vol. 44, No. 6, pp. 1243-1254*, 2006.

[2] Elizabeth K Benitez, Matthew P Borg, Jonathan L Hill, Anton Scholten, Pedro Paredes, and Joseph S Jewell. Measurements on a blunt cone-cylinder-flare at mach 6. *AIAA SciTech 2023 Forum, AIAA Paper 2023-1245*, 2023.

[3] Elizabeth K. Benitez, Sebastien Esquieu, Joseph S. Jewell, and Steven P. Schneider. Instability measurements on an axisymmetric separation bubble at mach 6. *AIAA Aviation 2020 Forum, AIAA Paper 2020-3072*, 2020.

[4] D. C. Berridge, K. M. Casper, S. J. Rufer, C. R. Alba, D. R. Lewis, S. J. Beresh, and S. P. Schneider. Measurements and computations of second-mode instability waves in three hypersonic wind tunnels. *AIAA Paper 2010-5002*, 2010.

[5] R. Bur and B. Chanetz. Experimental study on the pre-x vehicle focusing on the transitional shockwave/ boundary layer interactions. *Aerospace Science and Technology 13 (2009) 393–401*, 2009.

[6] Clément Caillaud, Mathieu Lugrin, Sebastien Esquieu, and Cedric Content. Global stability analysis of a hypersonic cone-cylinder-flare geometry. *Proceedings of the 57th 3AF International Conference on Applied Aerodynamics AERO 2023*, 2023.

[7] Sebastien Esquieu, Elizabeth Benitez, Steven P. Schneider, and Jean-Philippe Brazier. Flow and stability analysis of a hypersonic boundary layer over an axisymmetric cone cylinder flare configuration. *AIAA Scitech 2019 Forum, AIAA Paper 2019-2115*, 2019.

[8] Alexander Fedorov. Transition and stability of high speed boundary layers. *Annu. Rev. Fluid Mech. 2011. 43:79–95*, 2011.

[9] Heath B. Johnson and G. V. Candler. Hypersonic boundary layer stability analysis using pse-chem. *AIAA Paper 2005-5023*, 2005.

[10] J. M. Kendall. Wind tunnel experiments relating to supersonic and hypersonic boundary layer transition. *AIAA Journal, Vol.13, pp.290-299*, March 1975.

[11] Ivett A. Leyva. The relentless pursuit of hypersonic flight. *Physics Today*, 70:30, 36, 2017.

[12] Fei Li, Meelan M. Choudhari, Pedro Paredes, and Anton Scholten. Nonlinear evolution of instabilities in a laminar separation bubble at hypersonic mach number. *AIAA Aviation 2022 Forum, AIAA Paper 2022-3855*, 2022.

[13] Mathieu Lugrin, Samir Beneddine, Colin Leclercq, Eric Garnier, and Reynald Bur. Transition scenario in hypersonic axisymmetrical compression ramp flow. *Journal of Fluid Mechanics*, 907, 2020.

[14] Mathieu Lugrin, François Nicolas, Nicolas Severac, Jean-Pierre Tobeli, Samir Beneddine, Eric Garnier, Sebastien Esquieu, and Reynald Bur. Transitional shockwave/boundary layer interaction experiments in the R2Ch blowdown wind tunnel. *Experiments in Fluids*, 63(2):46, February 2022.

[15] Leslie M. Mack. Boundary-layer linear stability theory. *AGARD Report No. 709, Part 3*, 1984.

[16] Eric C. Marineau, George C. Moraru, Daniel R. Lewis, Joseph D. Norris, John F. Lafferty, and Heath B Johnson. Investigation of mach 10 boundary layer stability of sharp cones at angle-of-attack, part 1: Experiments. *53rd AIAA Aerospace Science Meeting, AIAA Paper 2015-1737*, 2015.

[17] M. V. Morkovin, E. Reshotko, and T. Herbert. Transition in open flow systems: a reassessment. *Bull. Am. Phys. Soc. 39:1882*, 1994.

[18] Pedro Paredes, Anton Scholten, Meelan M. Choudhari, Fei Li, Elizabeth K. Benitez, and Joseph S. Jewell. Boundary-layer instabilities over a cone–cylinder–flare model at mach 6. *AIAA Journal*, 60(10):5652–5661, 2022.

[19] Steven P. Schneider. Development of hypersonic quiet tunnels. *Journal of Spacecraft and Rockets*, 45(4), 641-664, 2008.

[20] Steven P. Schneider. Developing mechanism-based methods for estimating hypersonic boundary-layer transition in flight: The role of quiet tunnels. *Progress in Aerospace Sciences*, 72 (2015) 17-29, 2015.

[21] Kenneth F. Stetson. On predicting hypersonic boundary-layer transition. *Flight Dynamics Laboratory, AFWAL-TM-87-160-FIMG*, 1987.

[22] Kenneth F. Stetson. Comments on hypersonic boundary-layer transition. *Flight Dynamics Laboratory, WRDC-TR-90-3057*, 1990.

[23] J. E. Wuerer. Flow separation in high speed flight - a review of the state-of-the-art. *Douglas Report SM-46429, DTIC AD616216*, 1965.